telecom

MDPI

Article

Analytical Performance Evaluation of CP-OTFS for ISAC Under High-Doppler and Large-Delay Conditions

Sirine Hamrouni [1,2,*], Jean-Yves Baudais [2], Stéphane Méric [2] and Adnen Cherif [1]

[1] ATSSEE Laboratory, Faculty of Sciences of Tunis, University of Tunis El Manar, Tunis 2092, Tunisia; adnane.cherif@fst.utm.tn
[2] IETR Laboratory, Institut d'Électronique et des Technologies du numéRique, INSA Rennes, CNRS, 35700 Rennes, France; jean-yves.baudais@insa-rennes.fr (J.-Y.B.); stephane.meric@insa-rennes.fr (S.M.)
* Correspondence: sirine.hamrouni@insa-rennes.fr

Abstract

Orthogonal time-frequency space (OTFS) modulation is a promising waveform for integrated sensing and communication (ISAC) in high-mobility environments, where both large Doppler shifts and target delays must be accurately handled. Existing CP-OTFS radar analyses often assume CP-preserving target delays, for which the received echo remains inside the protected interval and CP-induced interference is avoided. However, practical sensing scenarios may involve large Doppler shifts and large target delays exceeding the cyclic-prefix duration, leading to CP violation and interference. This paper extends the analytical performance evaluation of cyclic-prefix OTFS (CP-OTFS) to this large-delay regime while also accounting for Doppler shifts. Starting from the CP-OTFS transmit signal, point-target channel, time-frequency demodulation, and delay-Doppler matched filtering, closed-form expressions are derived for the radar matched-filter output statistics, including the mean response, average delay-Doppler energy, main-lobe energy, peak sidelobe level ratio (PSLR), and integrated sidelobe level ratio (ISLR). For the communication function, an analytical error vector magnitude (EVM) expression is derived to quantify the degradation induced by large delays. The analytical expressions are evaluated as functions of target delay and Doppler shift and validated through end-to-end CP-OTFS ISAC simulations. The results demonstrate the accuracy of the analytical expressions and quantify the reduction in useful energy, the increase in interference, the degradation of the PSLR and ISLR, and the increase in EVM.

Keywords: OTFS; CP-OTFS; integrated sensing and communication; delay-Doppler domain; cyclic prefix; matched filter; PSLR; ISLR; EVM

Check for updates

Academic Editor: Michael Hempel

Received: 15 July 2026
Revised: 8 August 2026
Accepted: 19 August 2026
Published: 25 August 2026

Copyright: © 2026 by the authors. Licensee MDPI, Basel, Switzerland. This article is an open access article distributed under the terms and conditions of the Creative Commons Attribution (CC BY) license.

1. Introduction

Integrated sensing and communications (ISAC) has emerged as a key technology for future wireless networks, where radar sensing and data transmission are jointly performed using shared spectrum, hardware, and signal-processing resources [1,2]. This integration is motivated by the increasing demand for spectral efficiency, low-latency perception, and environment-aware communication in applications such as vehicular networks, unmanned aerial systems, and high-mobility wireless links. In such scenarios, the transmitted waveform must simultaneously provide reliable communication and accurate sensing of target delay and Doppler.

Orthogonal time-frequency space (OTFS) modulation has attracted significant attention as a candidate waveform for high-mobility communications and ISAC systems [3–7].

Unlike OFDM, which places information symbols directly in the time-frequency domain and becomes sensitive to Doppler-induced inter-carrier interference, OTFS modulates information in the delay-Doppler (DD) domain. This representation is particularly attractive for ISAC because the DD domain is naturally related to physical radar parameters: delay is associated with range, while Doppler is associated with radial velocity. As a result, OTFS provides a common signal representation for both communication over time-varying channels and radar sensing of moving targets. Representative applications include high-speed railway and vehicular links, UAV and airborne platforms, LEO satellite links, and long-range or multipath-rich sensing environments. In these scenarios, high relative velocities generate large Doppler shifts, while long propagation paths and multipath propagation produce large delays or delay spreads [8–11]. Several studies investigate OTFS-based ISAC systems. Early works demonstrate the effectiveness of OTFS for joint radar parameter estimation and communication, showing its potential for delay-Doppler sensing in high-mobility environments [12,13]. More recent works analyze OTFS sensing using ambiguity functions, matched-filter processing, and delay-Doppler estimation methods [6,7,14]. In particular, the ambiguity function of data-modulated OTFS signals is studied to characterize the effect of random communication symbols on radar sidelobes, including performance indicators such as the peak sidelobe level ratio (PSLR) and integrated sidelobe level ratio (ISLR) [14]. However, ambiguity-function-based analyses do not always directly describe the practical radar output obtained after receiver processing, though equivalence between both can be stated in particular cases [15]. For ISAC waveform design, it is therefore important to characterize the actual delay-Doppler matched-filter output, including its mean response, energy distribution, main-lobe behavior, and sidelobe statistics. Recent sensing research has also explored spatial-domain approaches based on flexible intelligent metasurfaces (FIMs). In [16], the transmitted signal and the three-dimensional FIM shape are jointly optimized to enhance the probing power toward multiple targets.

Most analytical OTFS radar studies assume that the received echo remains compatible with the cyclic-prefix structure of the transmitted frame and do not explicitly characterize the CP-violating case where the target delay exceeds the cyclic-prefix duration [13]. This corresponds to the CP-preserving regime. Under this assumption, the delayed echo is contained within the protected interval, the useful observation window keeps its circular structure, and there is no interference between adjacent symbols.

A preliminary radar-only analysis under the CP-preserving, no-interference assumption was presented in [17]. The present work extends this analysis to the CP-violating regime, where the target delay exceeds the cyclic-prefix duration, and additionally derives the communication EVM, thereby providing a joint sensing-and-communication performance characterization. However, practical sensing scenarios may involve large target delays, especially when the target range exceeds the protection provided by the cyclic prefix. In this case, the delayed echo is no longer fully absorbed by the CP, the circular CP-OTFS model is violated, and interference appears in both radar and communication processing.

Interference in OTFS systems is studied from several perspectives. In communication-oriented OTFS, rectangular pulse shaping, fractional Doppler, and delay-Doppler spreading generate inter-Doppler interference, inter-carrier interference (ICI), and inter-symbol interference (ISI), which motivate the development of interference cancellation and message-passing receivers [18]. In OTFS radar, ISI and ICI are also exploited rather than simply avoided, in order to extend the unambiguous sensing region and improve delay-Doppler estimation beyond conventional ambiguity limits [19]. More recently, MIMO-OTFS ISAC frameworks consider the effects of ISI and ICI on both sensing and communication performance [20]. Other works address mutual interference and DD-domain interference

suppression in ISAC systems [21]. These studies confirm that interference is a central issue in OTFS-based sensing and communication.

Nevertheless, the cited literature does not provide a joint closed-form characterization of CP-OTFS sensing and communication performance when the target delay exceeds the cyclic-prefix duration. This paper addresses this gap through the following contributions:

- We extend the analytical evaluation of CP-OTFS ISAC from the CP-preserving regime to the CP-violating regime while accounting for Doppler shifts;
- We derive closed-form expressions for the delay-Doppler radar matched-filter output statistics, including the mean response, average DD-map energy, main-lobe energy, PSLR, and ISLR;
- We derive a closed-form communication EVM expression to quantify the degradation caused by delay, Doppler shift, and CP violation;
- We validate the analytical expressions through end-to-end CP-OTFS ISAC simulations and characterize the joint EVM–PSLR performance tradeoff.

The paper is organized as follows. Section 2 introduces the considered CP-OTFS ISAC system model. Section 3 presents the analytical derivations of the radar performance metrics, and Section 4 presents the communication performance metrics. Section 5 validates the proposed expressions through numerical results. Section 6 discusses the ISAC performance tradeoffs. Section 7 provides a general discussion of the main findings. Finally, Section 8 concludes the paper.

2. System Model

This section presents the considered CP-OTFS ISAC system model illustrated in Figure 1. The transmit waveform is first constructed from QAM symbols placed in the delay-Doppler (DD) domain. These symbols are mapped to the time-frequency (TF) domain through the inverse symplectic finite Fourier transform (ISFFT) and then converted into a continuous-time CP-OTFS signal by an OFDM-type Heisenberg transform. At the receiver, the same received signal is used for both communication and radar sensing. The communication branch recovers the DD-domain data symbols, whereas the radar branch applies a matched-filter operation to form a delay-Doppler map. The considered framework is based on a dual-function CP-OTFS waveform transmitted for both communication and sensing. For communication, the emitted signal is received by a communication receiver, which demodulates the DD-domain data symbols. For sensing, two configurations can be considered. In the monostatic case, the sensing receiver is colocated with the transmitter and processes the echo reflected by the target. In the bistatic case, the sensing receiver is located on another platform and can process the target echo, assuming that the emitted CP-OTFS waveform is known.

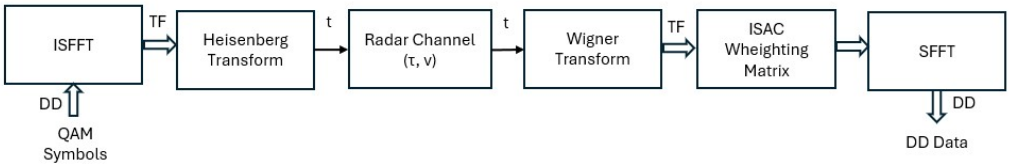


Figure 1. OTFS ISAC chain.

As illustrated in Figure 1, the delay–Doppler symbols are first transformed into the time–frequency domain and then converted into a time-domain signal using the OFDM modulation stage. A cyclic prefix is inserted before transmission and removed at the receiver before OFDM demodulation.

2.1. CP-OTFS Transmitter

Let $X_{\mathrm{DD}}[l,k]$ denote the information symbol located at delay index l and Doppler index k, where $l = 0, \cdots, M-1$ and $k = 0, \cdots, N-1$. The symbols are drawn from a QAM constellation and arranged on an $M \times N$ DD grid. The corresponding DD sampling lattice is

$$\Gamma_{\mathrm{DD}} = \left\{ \left(\frac{l}{M\Delta f}, \frac{k}{NT} \right),\ l = 0, \cdots, M-1,\ k = 0, \cdots, N-1 \right\}, \tag{1}$$

where T is the useful OTFS sub-symbol duration, and Δf is the subcarrier spacing. In this work, the orthogonality condition $\Delta f = 1/T$ is assumed. Hence, the occupied bandwidth is $B = M/T$, and each OTFS frame contains N multicarrier sub-symbols.

The DD-domain symbols are mapped to the TF domain using the ISFFT, as illustrated in the first block in Figure 1:

$$X_{\mathrm{TF}}[m,n] = \frac{1}{\sqrt{MN}} \sum_{k=0}^{N-1} \sum_{l=0}^{M-1} X_{\mathrm{DD}}[l,k] e^{j2\pi\left(\frac{nk}{N} - \frac{ml}{M}\right)}, \tag{2}$$

where $m = 0, \cdots, M-1$ and $n = 0, \cdots, N-1$ denote the subcarrier and time-slot indices, respectively. This transformation spreads each DD-domain symbol over the whole TF grid, which is the main mechanism through which OTFS exploits time and frequency diversity.

Let T_{CP} denote the cyclic-prefix duration and

$$T_s = T + T_{\mathrm{CP}} \tag{3}$$

the total duration of one CP-OTFS sub-symbol. The second block in Figure 1 denotes the continuous-time transmitted signal obtained through the Heisenberg transform, as

$$s(t) = \sum_{n=0}^{N-1} \sum_{m=0}^{M-1} X_{\mathrm{TF}}[m,n] g_{\mathrm{tx}}(t - nT_s) e^{j2\pi m \frac{t-nT_s}{T}}, \tag{4}$$

where $g_{\mathrm{tx}}(t)$ is the transmit pulse including the cyclic prefix. In this paper, it is a rectangular pulse defined as

$$g_{\mathrm{tx}}(t) = \begin{cases} 1, & 0 \le t < T_s, \\ 0, & \text{otherwise.} \end{cases} \tag{5}$$

Rectangular pulses were selected because they are commonly used in practical OFDM-based OTFS implementations and retain a simple transceiver structure based on FFT and IFFT processing together with cyclic-prefix insertion and removal. They also simplify the mathematical representation of the transmitted and received signals, enabling the effects of delay, Doppler shift, and CP violation to be analyzed in closed form [22].

The cyclic prefix preserves the circular structure of the multicarrier modulation when the propagation delay remains smaller than T_{CP}. When the target delay exceeds this duration, CP violation occurs, and interference appears in the received signal.

2.2. Delay-Doppler Channel Model

A monostatic sensing scenario with a normalized single isotropic point target is considered. This assumption enables the effects of the target delay, Doppler shift, and CP violation to be characterized independently of inter-target interference. The target is characterized by an isotropic complex coefficient h, a propagation delay τ, and a Doppler shift ν, that is modeled through the third block in Figure 1. The received baseband signal is modeled as [13]

$$r(t) = h\, s(t-\tau) e^{j2\pi\nu t} + b(t), \tag{6}$$

where $b(t)$ denotes additive white Gaussian noise. The delay τ determines the target range, while the Doppler shift ν is related to the radial velocity. In the CP-preserving regime, $\tau \leq T_{\mathrm{CP}}$, the delayed echo remains inside the protected interval. In the CP-violating regime, $\tau > T_{\mathrm{CP}}$, part of the delayed echo falls outside the cyclic prefix, which breaks the circular convolution and generates interference.

2.3. ISAC Receiver

At the receiver side, the signal $r(t)$ is first projected onto the TF domain using an OFDM-type demodulator. The receive window removes the cyclic prefix and keeps only the useful duration T. The Wigner tranform is used—the fourth block in Figure 1—and the TF-domain received samples are given by

$$Y_{\mathrm{TF}}[m,n] = \frac{1}{T}\int_{-\infty}^{\infty} r(t) g_{\mathrm{rx}}^{*}(t-nT_s) e^{-j2\pi m \frac{t-nT_s}{T}} dt, \tag{7}$$

where the receive window is adapted to the transmitted one, which is a rectangular pulse in this paper, and defined as

$$g_{\mathrm{rx}}(t) = \begin{cases} 1, & T_{\mathrm{CP}} \leq t < T_s, \\ 0, & \text{otherwise.} \end{cases} \tag{8}$$

The TF-domain samples are then processed according to the considered ISAC function. A unified TF-domain processing step, cf. the fifth block in Figure 1, can be written as

$$Z_{\mathrm{TF}}[m,n] = W_{\mathrm{TF}}[m,n] Y_{\mathrm{TF}}[m,n], \tag{9}$$

where $W_{\mathrm{TF}}[m,n]$ is a functionality-dependent weighting matrix.

For communication, no TF-domain matched filtering is applied, and the received TF samples are directly transformed back to the DD domain (The synchronization and equalization functions have to be applied before or after this DD transformation). Hence,

$$W_{\mathrm{TF}}[m,n] = 1. \tag{10}$$

For radar sensing, the receiver applies a TF-domain matched filter by multiplying the received TF samples by the conjugate of the transmitted TF symbols:

$$W_{\mathrm{TF}}[m,n] = X_{\mathrm{TF}}^{*}[m,n]. \tag{11}$$

Thus, the radar TF matched-filter output is

$$Z_{\mathrm{TF}}[m,n] = X_{\mathrm{TF}}^{*}[m,n] Y_{\mathrm{TF}}[m,n]. \tag{12}$$

Finally, the processed TF-domain samples are transformed into the DD domain using the SFFT, cf. the sixth block in Figure 1:

$$Z_{\mathrm{DD}}[l'',k''] = \frac{1}{\sqrt{MN}} \sum_{n=0}^{N-1} \sum_{m=0}^{M-1} Z_{\mathrm{TF}}[m,n] e^{-j2\pi\left(\frac{nk''}{N} - \frac{ml''}{M}\right)}. \tag{13}$$

where $l'' = 0, \cdots, M-1$ and $k'' = 0, \cdots, N-1$ For communication, $Z_{\mathrm{DD}}[l'',k'']$ represents the received DD-domain data symbols used for detection. For radar sensing, $Z_{\mathrm{DD}}[l'',k'']$

represents the delay-Doppler radar map. The target parameters are estimated from the location and amplitude of the dominant peak in this map.

3. Radar Analytical Derivations

This section presents the analytical performance evaluation for the radar point of view of the considered CP-OTFS ISAC system. The objective is to characterize, in closed form, how the delay-Doppler matched-filter output behaves when the target delay either is contained within the cyclic prefix or exceeds it. The analysis is based on the statistical properties of the random QAM data symbols and leads to analytical expressions for the mean DD-domain response, the average DD-map energy, the main-lobe energy, the sidelobe floor, the PSLR, and the ISLR.

The data symbols are assumed to be independent and identically distributed (i.i.d.) with zero mean, average energy $\sigma_X^2 = \mathbb{E}[|X_{\mathrm{DD}}[k,l]|^2]$, and fourth-order moment $\mu_X^4 = \mathbb{E}[|X_{\mathrm{DD}}[k,l]|^4]$. The noise is assumed to be complex circular Gaussian with variance σ_b^2. Unless otherwise stated, the analytical expressions are given for one like point-target described with a complex coefficient h, a delay τ, and a Doppler shift ν.

To explicitly account for the cyclic-prefix violation, we define

$$\tau_{\mathrm{CP}} = T_{\mathrm{CP}} + (\tau - T_{\mathrm{CP}})^+, \tag{14}$$

where $(x)^+ = \max(x, 0)$. Hence, when $\tau \leq T_{\mathrm{CP}}$, we have $\tau_{\mathrm{CP}} = T_{\mathrm{CP}}$, and the useful observation interval is CP-preserving. When $\tau > T_{\mathrm{CP}}$, we have $\tau_{\mathrm{CP}} = \tau$, meaning that the lower integration limit is shifted to the target delay.

3.1. Mean DD-Domain Matched-Filter Output

Since the OTFS frame is modulated by random QAM data symbols, the DD-domain matched-filter output is a random quantity. Its expectation provides the coherent, data-averaged radar response. Starting from the expanded matched-filter expression $Z_{\mathrm{DD}}[l'', k'']$ given in Appendix A, the expectation is obtained by averaging over the random DD-domain symbols. Since the transmitted symbols are assumed i.i.d. and zero mean, they satisfy

$$\mathbb{E}\left[X_{\mathrm{DD}}[l,k]X_{\mathrm{DD}}^*[l',k']\right] = \sigma_X^2 \delta_{l,l'}\delta_{k,k'}. \tag{15}$$

Therefore, only the terms with identical DD indices remain after averaging, i.e., $l = l'$ and $k = k'$. The noise contribution has zero mean and does not contribute to the expected matched-filter output, then

$$\mathbb{E}\left[Z_{\mathrm{DD}}[l'', k'']\right] = \frac{\sigma_X^2 h}{T\sqrt{MN}} e^{-j2\pi\nu\tau} \sum_{n=0}^{N-1} e^{j2\pi n\left(\nu T_s - \frac{k''}{N}\right)} \sum_{m=0}^{M-1} e^{j2\pi m\left(\frac{l''}{M} - \frac{\tau}{T}\right)} \int_{\tau_{\mathrm{CP}}}^{T_s} e^{j2\pi\nu u} du. \tag{16}$$

This equation shows that the radar response is governed by three factors: a Doppler-dependent slow-time summation over the N OTFS symbols, a time-domain integration over the useful received interval, and a delay-dependent frequency summation over the M subcarriers. The CP violation appears explicitly through the lower integration limit τ_{CP}. When $\tau \leq T_{\mathrm{CP}}$, the integration length is $T_s - T_{\mathrm{CP}} = T$, corresponding to the full useful symbol duration. In contrast, when $\tau > T_{\mathrm{CP}}$, the integration length becomes $T_s - \tau < T$. Therefore, only part of the delayed echo contributes coherently to the matched-filter output, which reduces the main-lobe amplitude.

However, the expectation alone is not sufficient to evaluate the sidelobe behavior. Due to the averaging over random data symbols, the sidelobe terms vanish for on-grid delay-

Doppler (DD) shifts. Therefore, the PSLR and ISLR must be derived from the second-order moment $\mathbb{E}\left[|Z_{\mathrm{DD}}[l'',k'']|^2\right]$, which preserves the average sidelobe energy.

3.2. Mean DD-Map Energy

The average DD-map energy is defined as $\mathbb{E}\left[|Z_{\mathrm{DD}}[l'',k'']|^2\right]$. This quantity describes the average energy distribution of the radar map and forms the basis for the analytical derivation of the main-lobe and sidelobe metrics.

We first define:

$$\mathcal{D}_Q(x) = \frac{\sin(\pi Q x)}{\sin(\pi x)}, \tag{17}$$

and the useful coherent integration factor

$$\mathcal{G}(\nu,\tau_{\mathrm{CP}}) = \left|\frac{1}{T}\int_{\tau_{\mathrm{CP}}}^{T_s} e^{j2\pi\nu u}du\right|^2 = \left(\frac{T_s-\tau_{\mathrm{CP}}}{T}\right)^2 \mathrm{sinc}^2\left(\nu(T_s-\tau_{\mathrm{CP}})\right), \tag{18}$$

where $\mathrm{sinc}(x) = \sin(\pi x)/(\pi x)$. Physically, $\mathcal{G}(\nu,\tau_{\mathrm{CP}})$ quantifies the target-response energy retained over the useful observation interval. When the delay exceeds the CP, this interval becomes shorter, reducing the radar energy, while the sinc term accounts for the additional loss caused by the Doppler-induced phase rotation.

The auxiliary functions associated with the two received signal contributions are defined as

$$\Psi_A(l,m) = \sum_{m=0}^{M-1} e^{j2\pi m\frac{l+l''}{M}}\Phi_A(l,m), \tag{19}$$

and

$$\Psi_B(l,m) = \sum_{m=0}^{M-1} e^{j2\pi m\frac{l+l''}{M}}\Phi_B(l,m), \tag{20}$$

where

$$\Phi_A(l,m) = e^{j2\pi\nu\tau}e^{-j2\pi m\tau/T}\sum_{m'=0}^{M-1} e^{-j2\pi m' l/M}\frac{T-\tau}{T}e^{j\pi\left(\nu+\frac{m'-m}{T}\right)(T-\tau)}\,\mathrm{sinc}\left(\left(\nu+\frac{m'-m}{T}\right)(T-\tau)\right), \tag{21}$$

and

$$\Phi_B(l,m) = \sum_{m'=0}^{M-1} e^{-j2\pi m'\left(\frac{\tau}{T}+\frac{l}{M}\right)}\frac{\tau}{T}e^{j\pi\left(\nu+\frac{m'-m}{T}\right)\tau}\,\mathrm{sinc}\left(\left(\nu+\frac{m'-m}{T}\right)\tau\right). \tag{22}$$

Using the definitions (17)–(20), the average DD-map energy is obtained as

$$\begin{aligned}\mathbb{E}\left[|Z_{\mathrm{DD}}[l'',k'']|^2\right] = {} & \underbrace{\frac{\sigma_X^4|h|^2}{M^2}\sum_{l=0}^{M-1}\sum_{m=0}^{M-1}\left(|\Phi_A(l,m)|^2+|\Phi_B(l,m)|^2\right)}_{(a)} + \underbrace{\frac{\sigma_X^4|h|^2}{MN}\mathcal{G}(\nu,\tau_{\mathrm{CP}})\left|\mathcal{D}_N\left(\nu T_s-\frac{k''}{N}\right)\right|^2\left|\mathcal{D}_M\left(\frac{l''}{M}-\frac{\tau}{T}\right)\right|^2}_{(b)} \\ & + \underbrace{\frac{\mu_X^4-2\sigma_X^4}{M^3N^2}|h|^2\left|\mathcal{D}_N\left(\nu T_s-\frac{k''}{N}\right)\right|^2\sum_{l=0}^{M-1}\left(|\Psi_A(l,m)|^2+|\Psi_B(l,m)|^2\right)}_{(c)} + \underbrace{\sigma_X^2\sigma_b^2}_{(d)}.\end{aligned} \tag{23}$$

A detailed derivation is provided in Appendix A. The first and third terms, (a) and (c), respectively, describe the energy fluctuations induced by random data modulation, while the second term (b) corresponds to the coherent target-dependent contribution. The last term (d) is the noise contribution after matched filtering. The expression explicitly depends on the delay τ, Doppler shift ν, CP duration T_{CP}, and OTFS grid dimensions M and N.

3.3. Main-Lobe Energy

For the on-grid case, the target main lobe is located on the DD grid

$$l_0'' = \frac{M\tau}{T}, \qquad k_0'' = N\nu T_s. \tag{24}$$

By evaluating (23) at the target-aligned bin (l_0'', k_0''), the average main-lobe energy is obtained as

$$\begin{aligned} E_{\mathrm{ML}} = {} & \frac{\sigma_X^4|h|^2}{M^2}\sum_{l=0}^{M-1}\sum_{m=0}^{M-1}\left(|\Phi_A(l,m)|^2 + |\Phi_B(l,m)|^2\right) + \sigma_X^4|h|^2 MN\left(\frac{T_s-\tau_{\mathrm{CP}}}{T}\right)^2 \mathrm{sinc}^2\left(\nu(T_s-\tau_{\mathrm{CP}})\right) \\ & + \frac{\mu_X^4 - 2\sigma_X^4}{M^3}|h|^2\sum_{l=0}^{M-1}\left(|\Psi_A(l,m)|^2 + |\Psi_B(l,m)|^2\right) + \sigma_X^2\sigma_b^2. \end{aligned} \tag{25}$$

In this equation, the coherent part corresponds to the main lobe that contains the point target response with the factor $\left(\frac{T_s-\tau_{\mathrm{CP}}}{T}\right)^2 \mathrm{sinc}^2(\nu(T_s-\tau_{\mathrm{CP}}))$. This term has a direct physical interpretation. The factor $T_s - \tau_{\mathrm{CP}}$ represents the effective coherent integration duration. Therefore, when the delay exceeds the cyclic prefix, the coherent integration interval decreases, which reduces the main-lobe energy. In addition, the sinc term describes the Doppler-induced loss due to phase rotation during the observation interval.

For the off-grid case, the target response is spread on the DD map, due to the sinc function patterns as described in (21) and (22).

3.4. Average Sidelobe Energy

The average sidelobe energy is obtained directly by evaluating the mean energy expression (23) at the DD bins different from the target-aligned bin, i.e., $(l'', k'') \neq (l_0'', k_0'')$. The sidelobe energy distribution is well represented by an exponential one [23], as illustrated in Figure 2. The close agreement between the simulated probability density and the analytical exponential distribution confirms the accuracy of this statistical approximation for the sidelobe energy. Let λ denotes the parameter of this distribution. The average sidelobe energy is then equal to $1/\lambda$. In the case of off-grid DD, (23) is used to calculate the sidelobe energy, and, in the case of on-grid DD, the analytical sidelobe floor is given by

$$\begin{aligned} E_{\mathrm{SL}} = {} & \frac{\sigma_X^4|h|^2}{M^2}\sum_{l=0}^{M-1}\sum_{m=0}^{M-1}\left(|\Phi_A(l,m)|^2 + |\Phi_B(l,m)|^2\right) \\ & + \frac{\mu_X^4 - 2\sigma_X^4}{M^3}|h|^2\delta_{k''k_0''}\sum_{l=0}^{M-1}\sum_{m=0}^{M-1}\left(|\Psi_A(l,m)|^2 + |\Psi_B(l,m)|^2\right) + \sigma_X^2\sigma_b^2, \end{aligned} \tag{26}$$

where $\delta_{k''k_0''}$ is the Kronecker function.

3.5. PSLR and ISLR

The peak sidelobe level ratio is defined as the ratio between the main-lobe energy and the maximum sidelobe energy:

$$\mathrm{PSLR} = \frac{\mathbb{E}\left[\left|Z_{\mathrm{DD}}[l_0'', k_0'']\right|^2\right]}{\mathbb{E}\left[\max\limits_{(l'',k'')\neq(l_0'',k_0'')}\left|Z_{\mathrm{DD}}[l'', k'']\right|^2\right]}. \tag{27}$$

Using the exponential approximation of the sidelobe samples, the expected maximum sidelobe energy is approximated through the harmonic factor H_{MN-1} [23] (App. C),

$$\mathbb{E}\left[\max_{(l'',k'')\neq(l_0'',k_0'')}\left|Z_{\mathrm{DD}}[l'',k'']\right|^2\right] = H_{MN-1}E_{\mathrm{SL}}, \tag{28}$$

where

$$H_{MN-1} = \sum_{q=1}^{MN-1}\frac{1}{q}. \tag{29}$$

Therefore, the analytical PSLR is

$$\mathrm{PSLR} = \frac{E_{\mathrm{ML}}}{H_{MN-1}E_{\mathrm{SL}}}. \tag{30}$$

With the same main-lobe-to-sidelobe convention, the ISLR is defined as the ratio between the main-lobe energy and the total sidelobe energy. It can also be expressed in closed-form as a linear function of the PSLR, as reported in ([23] (30)),

$$\mathrm{ISLR} = \frac{E_{\mathrm{ML}}}{(MN-1)E_{\mathrm{SL}}} = \mathrm{PSLR}\frac{H_{MN-1}}{MN-1}. \tag{31}$$

The radar sidelobe metrics are controlled by the competition between the coherent main-lobe energy and the average sidelobe floor, as shown by (30) and (31).

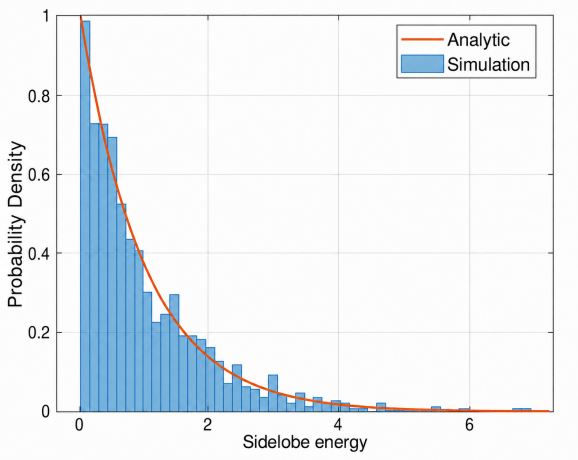


Figure 2. Probability density of the sidelobe energy: analytical exponential distribution and Monte Carlo simulation. Simulation parameters: $M = 128$, $N = 16$, $T_{\mathrm{CP}} = 8T/M$, $h = 1$, SNR = 20 dB, and 1000 Monte Carlo realizations.

4. Communication Analytical Derivations

The communication performance is evaluated through the error vector magnitude. This EVM is computed from the demodulated DD-domain symbols. Let $\widehat{X}_{\mathrm{DD}}[k,l]$ denote the demodulated DD symbol and $X_{\mathrm{DD}}[k,l]$ the transmitted DD symbol. The mean-squared EVM is defined as

$$\gamma^2_{\mathrm{EVM}} = \frac{1}{MN\sigma_X^2}\sum_{k'=0}^{N-1}\sum_{l'=0}^{M-1}\mathbb{E}\left[\left|\widehat{X}_{\mathrm{DD}}[k,l] - X_{\mathrm{DD}}[k,l]\right|^2\right]. \tag{32}$$

By examining the term A_M in the asymptotic regime, it is found to converge to unity, as shown in (A23). Therefore, for sufficiently large values of M, A_M can be approximated by one, leading to (33).

$$\gamma^2_{\mathrm{EVM}} = \frac{\sigma_b^2}{\sigma_X^2} + 2 - \frac{2}{M}\mathcal{D}_M\left(\frac{\tau}{T}\right)\frac{1}{N}\mathcal{D}_N(\nu T_s)\sqrt{\mathcal{G}(\nu,\tau_{\mathrm{CP}})}\cos\left[\pi\left((N-1)\nu T_s - \frac{(M-1)\tau}{T} + \nu(T+\tau_{\mathrm{CP}}-T_{\mathrm{CP}})\right)\right], \tag{33}$$

where $\tau_{\mathrm{CP}} - T_{\mathrm{CP}}$ explicitly represents the part of the delay that exceeds the cyclic prefix. Therefore, when $\tau \leq T_{\mathrm{CP}}$, we have $\tau_{\mathrm{CP}} - T_{\mathrm{CP}} = 0$, and the expression reduces to the CP-preserving case. When $\tau > T_{\mathrm{CP}}$, the CP-exceeding delay modifies the EVM through the function $\mathcal{G}$ (18) and cosine terms, showing that CP violation directly affects the demodulated communication symbols. Physically, Equation (33) measures the average distortion between the transmitted and demodulated DD-domain symbols. The first term represents the noise contribution, while the remaining terms account for the mismatch caused by residual delay and Doppler after synchronization. Larger residual errors therefore lead to a higher EVM. In the asymptotic regime, when $M, N \to \infty$, some terms vanish and the squared EVM converges

$$\lim_{M,N\to\infty} \gamma^2_{\mathrm{EVM}} = \frac{\sigma_b^2}{\sigma_X^2} + 2. \tag{34}$$

This asymptotic expression must be interpreted carefully. This limit is taken for fixed T. Thus, increasing M reduces the DD-sample duration T/M. While the delay τ is fixed, this delay becomes more severe relative to the DD sample duration. All of this explains the non-zero asymptotic EVM floor.

5. Numerical Results

This section validates the analytical expressions derived in Sections 3 and 4 through end-to-end CP-OTFS ISAC simulations. The objective is to evaluate the accuracy of the proposed closed-form results and to analyze the impact of delay τ, Doppler ν, SNR $\frac{\sigma_X^2}{\sigma_b^2}$, and cyclic-prefix violation on the radar and communication performances. The radar performance is assessed using the PSLR, while the communication performance is evaluated using the EVM. The analytical expressions are compared with Monte Carlo simulations obtained from the complete CP-OTFS ISAC processing chain, cf. Figure 1 using 1000 Monte Carlo realizations, with $h = 1$, $M = 128$, $N = 16$, and $T_{\mathrm{CP}} = 8T/M$. The SNR, delay, and Doppler values are varied according to the scenario considered in each figure.

Figure 3 shows the PSLR as a function of the normalized target delay τ/T for different Doppler-bin indices k_0'' (24). The relatively high SNR of 40 dB is selected to reduce the influence of noise and highlight the effects of delay and Doppler on the PSLR. The vertical dashed line in the delay-dependent figures indicates the cyclic-prefix limit, i.e., $\tau = T_{\mathrm{CP}}$. Therefore, the region located on the left of this line corresponds to the CP-preserving regime, while the region located on the right corresponds to the CP-violating regime. A very close agreement is observed between the analytical expressions and the simulation results over the whole delay range, which validates the proposed PSLR derivation. For the zero-Doppler case, i.e., $k_0'' = 0$, a small gap of about 0.3 dB is observed at low delays between the analytical and simulation results. Since this difference is very small compared with the overall PSLR variation, the analytical trend remains valid. For small delays, i.e., when the target delay remains inside the CP duration, the PSLR is almost constant. This confirms that, in the CP-preserving regime, the delayed echo remains protected by the cyclic prefix and the DD matched-filter output is only weakly affected by the delay.

When τ exceeds T_{CP}, the PSLR starts to decrease. This degradation becomes more pronounced as the delay increases. This behavior is consistent with the analytical expressions of the main-lobe and sidelobe energies: CP violation reduces the effective coherent

integration interval and introduces additional interference, which simultaneously decreases the main-lobe energy and increases the sidelobe floor. Consequently, the peak becomes less dominant with respect to the sidelobes. The figure also shows that the Doppler value affects the PSLR level. For higher Doppler bins, the PSLR is lower because the Doppler-induced phase rotation reduces coherent accumulation in the matched-filter output.

Figure 4 presents the PSLR versus SNR for the two delay regimes: $\tau \leq T_{\mathrm{CP}}$ and $\tau > T_{\mathrm{CP}}$. The analytical and simulated curves are again in good agreement, which confirms that the proposed model correctly captures both noise-limited and interference-limited behaviors. For the CP-protected region, i.e., $\tau \leq T_{\mathrm{CP}}$, a small gap of about 0.3 dB is also observed between the analytical and simulation results at high SNR. At low SNR, the PSLR is mainly limited by noise. Therefore, increasing the SNR improves the PSLR for both delay regimes. However, this improvement becomes progressively smaller at high SNR, where the PSLR tends to saturate. This saturation indicates that the sidelobe level is no longer dominated by thermal noise, but only by the intrinsic random-data sidelobes and, in the CP-violating case, by the additional interference.

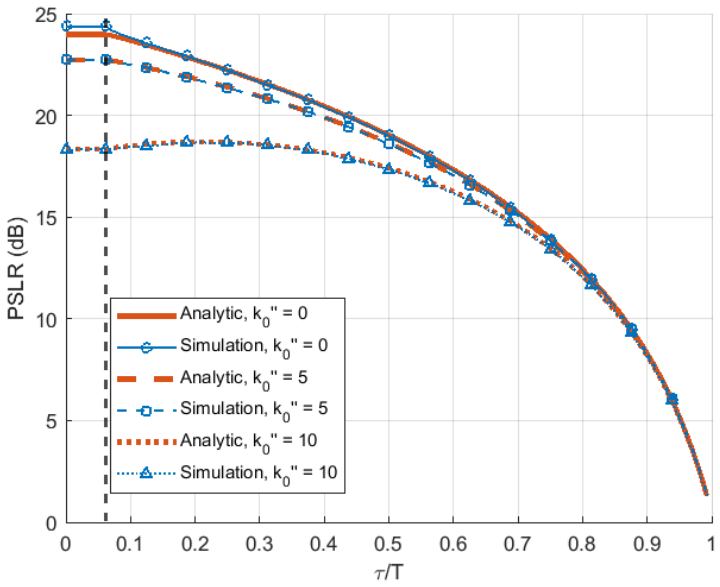


Figure 3. Analytical and simulated PSLR versus normalized delay τ/T for different Doppler-bin indices. The vertical dashed line indicates the CP limit. Simulation parameters: $M = 128$, $N = 16$, $T_{\mathrm{CP}} = 8T/M$, $h = 1$, SNR $= 40$ dB, and 1000 Monte Carlo realizations.

The comparison between the two delay regimes clearly shows the effect of CP violation. For the same SNR, the PSLR obtained with $\tau > T_{\mathrm{CP}}$ is lower than that obtained with $\tau \leq T_{\mathrm{CP}}$. This confirms that a delay exceeding the cyclic prefix degrades the radar map even when the noise level is reduced. In other words, increasing SNR cannot fully compensate for the interference created by CP violation.

Figure 5 illustrates the PSLR versus normalized Doppler νT. The analytical and simulation results are nearly superimposed for both $\tau \leq T_{\mathrm{CP}}$ and $\tau > T_{\mathrm{CP}}$, which validates the Doppler-dependent terms of the proposed analysis. For small normalized Doppler values, the PSLR remains high because the received echo stays nearly coherent over the OTFS frame. As νT increases, the PSLR decreases due to the loss of coherent integration caused by Doppler-induced phase rotation. This behavior is consistent with the sinc-type Doppler dependence of the main-lobe energy derived in Section 3.

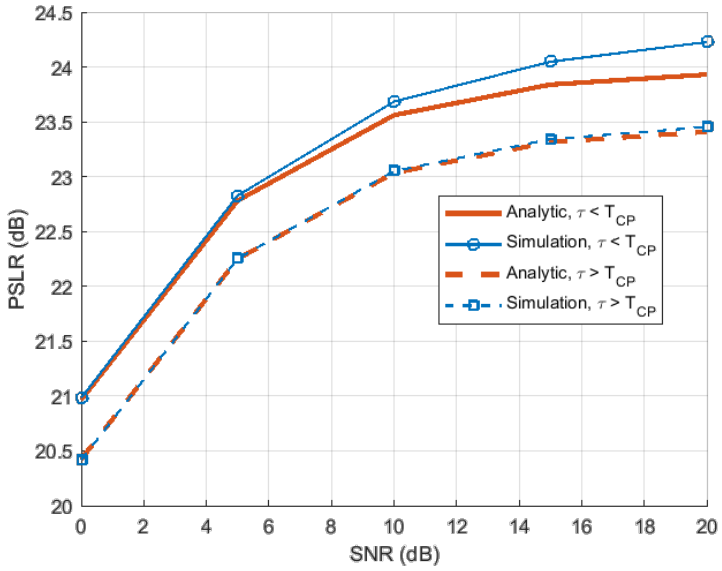


Figure 4. Analytical and simulated PSLR versus SNR for the CP-preserving case $\tau \leq T_{CP}$ and the CP-violating case $\tau > T_{CP}$.

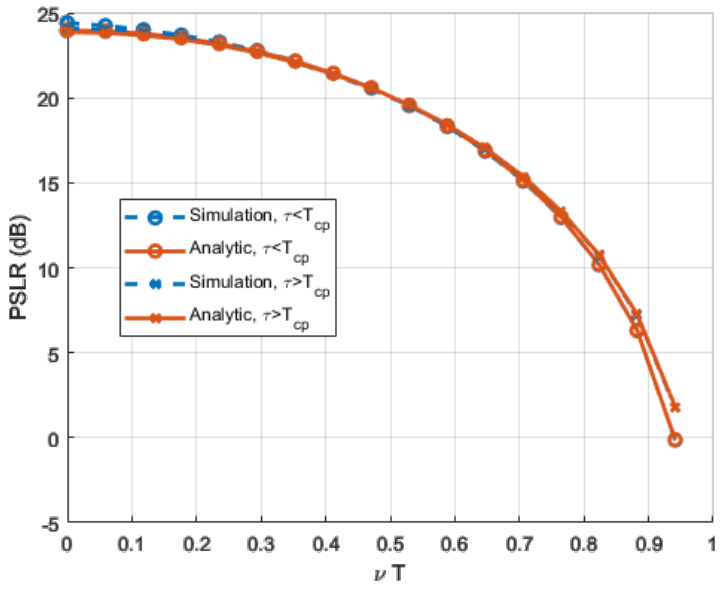


Figure 5. Analytical and simulated PSLR versus normalized Doppler νT for the CP-preserving and CP-violating regimes.

Figure 6 shows the PSLR versus normalized delay for different SNR values. In the CP-preserving region, the PSLR remains approximately constant for each SNR value. This confirms that, when the delay is absorbed by the cyclic prefix, the radar response is not significantly affected by the target delay. The difference between the curves is mainly due to the noise level: higher SNR values produce higher PSLR because the noise contribution in the sidelobe floor is reduced.

After the CP limit, the PSLR decreases for all SNR values. This decrease confirms the analytical prediction that CP violation introduces additional interference and reduces the effective coherent integration length. At low SNR, the PSLR is limited by both noise and interference. At high SNR, the curve remains higher, but it still decreases with delay because the dominant impairment becomes CP-induced interference rather than noise. This result is important because it shows that the degradation caused by large target delays cannot be removed only by increasing the transmit power or SNR.

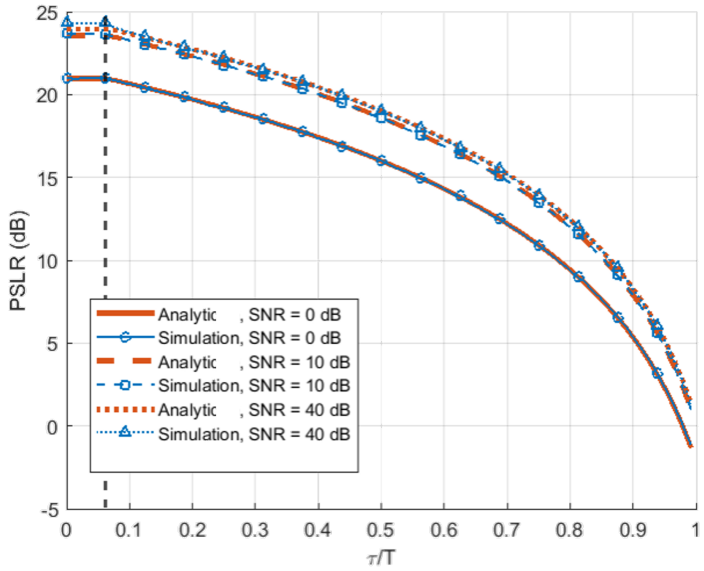


Figure 6. Analytical and simulated PSLR versus normalized delay τ/T for different SNR values.

Figure 7 shows the analytical and simulated EVM as a function of the normalized residual delay τ/T, for different normalized residual Doppler values νT (33). The delay range is limited to $\tau/T \leq 0.01$ because the communication delay considered here is a residual delay, assumed to be equal to 1% of the sensing delay. At $\tau/T = 0$ and $\nu T = 0$, the EVM is mainly limited by the noise level. Therefore, for SNR $= 20$ dB, the EVM starts around -20 dB, which corresponds to the noise floor. When the residual Doppler increases, the EVM is already degraded at zero delay due to the Doppler-induced distortion. As the residual delay increases, the EVM rapidly increases because the received DD-domain symbols become less aligned with the transmitted ones. The EVM reaches its maximum value when $\tau/T = 1/M = 0.0078$, which corresponds to one DD-domain symbol size. A good agreement between the analytical expression and the Monte-Carlo simulation is observed over the considered delay range that validates (33).

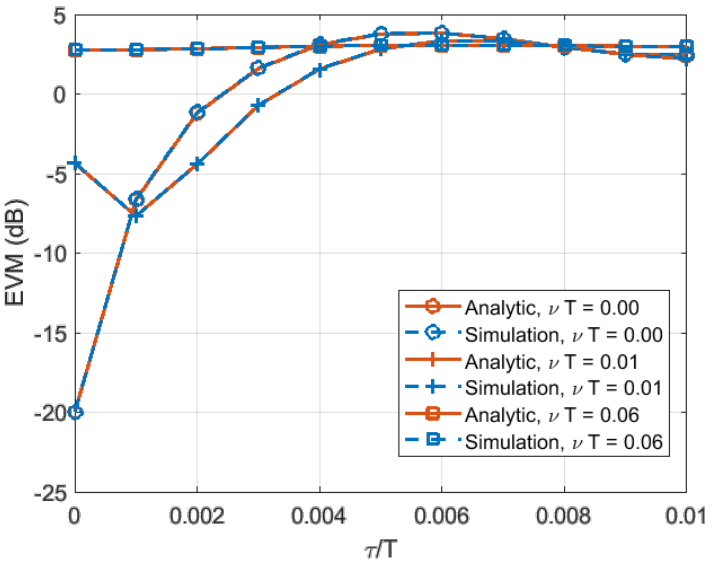


Figure 7. Analytical and simulated EVM versus normalized delay τ/T, for three Doppler shifts.

Overall, the results show that the system behavior differs before and after CP violation. When the delay remains within the cyclic prefix, the PSLR is mainly affected by noise and Doppler. When the delay exceeds the cyclic prefix, additional interference reduces the co-

herent radar contribution and increases the sidelobe level, which degrades the PSLR even at high SNR. For communication, residual delay and Doppler increase the mismatch between transmitted and received DD-domain symbols and consequently increase the EVM.

6. ISAC Performances

Figure 8 shows the ISAC performance in the EVM–PSLR plane for a fixed cyclic prefix duration $T_{\mathrm{CP}} = 8T/M$ and zero Doppler shift. The figure is obtained by evaluating the analytical PSLR and EVM expressions for the same set of target delays, with $M = 128$, $N = 16$, $h = 1$, and SNR $= 20$ dB. The considered normalized target delays are $\tau/T = \{0.02, 0.05, 0.06, 0.08, 0.09\}$. The radar PSLR is evaluated as a function of the target delay τ, whereas the communication EVM is computed using a residual delay equal to 0.01τ. For each value of τ, the corresponding EVM and PSLR values form one operating point in the EVM–PSLR plane. The blue markers correspond to the CP-protected regime, where $\tau \leq T_{\mathrm{CP}}$, while the orange markers indicate the CP-violating regime. In the CP-protected region, the PSLR remains almost constant, which shows that the radar main-lobe-to-sidelobe contrast is preserved as long as the target echo remains within the cyclic prefix. At $\tau/T = T_{\mathrm{CP}}/T$, the curve reaches the CP limit. Beyond this point, the PSLR starts to decrease, reflecting the degradation of the radar response caused by CP violation. At the same time, the EVM increases because the residual delay also increases with τ. However, in the considered range, the residual delay remains below $1/M$, so the EVM has not yet reached its saturation region, where it becomes approximately constant. This figure therefore highlights the trade-off between communication and radar performance.

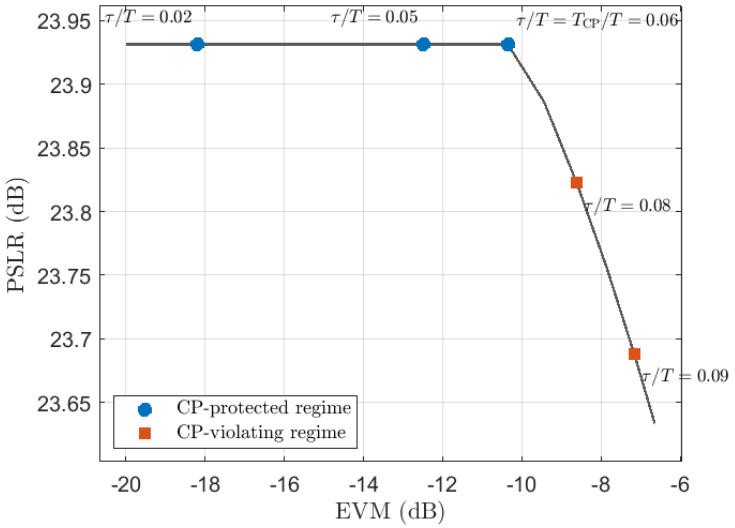


Figure 8. Analytical ISAC performance trade-off between the EVM and the radar PSLR.

7. Discussion

The numerical results provide several important insights into the behavior of CP-OTFS ISAC under high-Doppler and large-delay conditions. First, the close agreement between the analytical curves and the Monte Carlo simulations confirms the validity of the proposed statistical framework. In particular, the derived expressions accurately capture the evolution of the PSLR with respect to target delay, Doppler shift, and SNR. This agreement also validates the assumptions used in the derivation, including the statistical modeling of the random DD-domain data symbols and the separation between the coherent main-lobe contribution and the random sidelobe floor.

A key observation is that the CP-preserving and CP-violating regimes lead to clearly different radar behaviors. When the target delay remains below the cyclic-prefix duration,

the PSLR is not affected by the delay. In this region, the delayed echo remains compatible with the circular structure of the CP-OTFS frame, and the useful coherent integration is preserved. As a result, the DD-domain radar map keeps a dominant main lobe and relatively low sidelobe levels. This confirms the validity of the classical CP-preserving assumption used in many OTFS radar analyses.

In contrast, when the delay exceeds the cyclic prefix, the PSLR decreases significantly. This degradation is explained by the fact that the CP-violating part of the delayed echo introduces additional interference, which increases the sidelobe floor. The PSLR degradation is therefore not only a noise effect, but a structural effect caused by the loss of the CP-induced circularity. This explains why increasing the SNR improves the PSLR only up to a certain point and cannot fully compensate for the degradation caused by large target delays.

From the communication perspective, the EVM exhibits a different behavior because it is evaluated using the residual delay, taken here as 0.01τ. Therefore, the communication degradation evolves on a smaller delay scale than the radar degradation. For small residual delays, the EVM is mainly limited by the noise level, which explains its low value at high SNR. As τ increases, the residual delay also increases, producing a progressive mismatch in the demodulated DD-domain symbols and, consequently, an increase in the EVM. However, as long as the residual delay remains below the delay resolution $1/M = 1/128$, the EVM has not yet reached its saturation region. Beyond this limit, the delay-induced distortion no longer increases significantly, and the EVM tends to become approximately constant. This behavior explains why, in the EVM–PSLR representation, the PSLR starts to degrade once the target delay exceeds the cyclic prefix, while the EVM may still continue to increase before reaching its saturation level.

High Doppler and CP violation affect the system through different mechanisms. When the delay remains within the cyclic prefix, increasing Doppler causes a gradual loss of coherent accumulation, which reduces the radar main-lobe energy and increases the EVM. In contrast, when the delay exceeds the cyclic prefix, the circular signal structure is broken, and additional interference is introduced. This causes a sharper increase in the sidelobe level and degrades the PSLR and ISLR. When both effects occur simultaneously, the Doppler-induced coherent loss is combined with the interference caused by CP violation, leading to further degradation of both radar and communication performance. Therefore, CP violation is mainly responsible for the sharp degradation beyond the CP limit, while high Doppler produces an additional gradual degradation.

These observations are consistent with previous OTFS sensing and ISAC studies showing the relevance of DD-domain processing under high mobility [12,14,20]. However, while these studies mainly investigate radar parameter estimation, ambiguity-function behavior, or ISI/ICI exploitation, the present analysis explicitly quantifies the effect of CP violation on the DD-domain matched-filter output, PSLR/ISLR, and communication EVM.

In a multi-target or multipath scenario, the DD-domain matched-filter output is the linear superposition of the individual target or path responses. However, the corresponding second-order statistics also contain pairwise cross terms that depend on the targets' amplitudes, relative phases, delays, Doppler shifts, and separations in the delay-Doppler domain. For sufficiently separated targets, the proposed single-target expressions may provide a local approximation around each resolved target peak. In contrast, closely spaced or strongly unequal targets may produce overlapping responses, allowing the sidelobes of a strong target to mask a weaker target and consequently modify the target-specific PSLR and ISLR [12,20]. The results derived in this work should therefore be interpreted as reference bounds for an isolated target. A complete multi-target analysis would require

a specific scene model defining the number of targets, their amplitudes, phases, delays, Doppler shifts, and relative delay-Doppler separations, and is left for future work.

Although rectangular pulses simplify the implementation of the OFDM-based OTFS transceiver and the derivation of closed-form expressions, their limited frequency localization leads to relatively high out-of-band emissions [24,25]. Raised-cosine and root-raised-cosine pulse shaping can improve spectral confinement and, with an appropriate roll-off factor, may reduce interference associated with fractional delays [24,26]. However, these pulse shapes do not increase the cyclic-prefix duration. Therefore, when $\tau > T_{\mathrm{CP}}$, part of the received echo remains outside the protected interval, and RC/RRC pulse shaping alone cannot eliminate the interference caused by CP violation. Moreover, changing the pulse shape changes the mathematical representation of the received OTFS signal. Consequently, the DD-domain statistics and the corresponding PSLR and ISLR expressions must be derived again for the selected pulse shape and roll-off factor [24,26]. This extension is left for future work.

The main limitations of the proposed model are the single point-target model with additive white Gaussian noise and the use of rectangular transmit and receive pulses. Multiple targets or multipath components and alternative pulse shapes may introduce additional cross-interference and modify the sidelobe structure beyond that captured by the present single-target expressions. The results are therefore mainly applicable as performance-prediction tools for CP-OTFS ISAC systems operating under the stated assumptions, particularly in high-mobility and long-range sensing scenarios.

From a system-design perspective, these results highlight the importance of choosing the cyclic-prefix duration according to the expected sensing range. A short CP improves spectral efficiency but increases the probability of CP violation for distant targets.

The proposed analytical expressions make this tradeoff explicit by linking T_{CP}, target delay, Doppler shift, main-lobe energy, sidelobe energy, and PSLR in closed form. They can therefore be used as design tools by evaluating candidate system parameters against prescribed sensing and communication requirements. For given maximum delay and Doppler conditions, the closed-form expressions can be used to select the minimum T_{CP} and required SNR satisfying target PSLR and EVM thresholds, and to compare candidate values of M and N. The EVM expression can also be used to determine the residual delay and Doppler accuracy required after synchronization. A complete joint optimization of these parameters and the associated overhead is beyond the scope of this work and is left for future research.

Because the high-SNR performance floor originates from CP-induced interference rather than additive noise, mitigation techniques should either reduce the interfering contribution or prevent CP violation. First, time-frequency-domain windowing may reduce delay-Doppler leakage and suppress some interference components, although it cannot by itself restore the circular signal structure when $\tau > T_{\mathrm{CP}}$ and may introduce a tradeoff between interference suppression and coherent processing gain [27]. Second, model-based interference cancellation could exploit the estimated delay, Doppler shift, and target gain to reconstruct and subtract the CP-violating contribution before delay-Doppler matched filtering or communication detection. Iterative interference-cancellation and interference-aware detection methods have already demonstrated their relevance for OTFS receivers [18,21]; however, their effectiveness depends on parameter-estimation accuracy and entails additional computational complexity. Finally, the CP duration could be adapted according to the expected maximum propagation or sensing delay, thereby maintaining $\tau \leq T_{\mathrm{CP}}$ for the protected operating range. This approach directly prevents CP violation but increases guard-interval overhead and reduces spectral efficiency [28]. The joint optimization and

quantitative evaluation of these mitigation strategies under sensing-range, complexity, and communication-throughput constraints constitute relevant directions for future work.

The present work considers full-CP OTFS, where a cyclic prefix is added to each OTFS subsymbol. In reduced-CP OTFS, only one CP is added to the whole OTFS symbol, which reduces the CP overhead [24]. In ZP-OTFS, zero padding is used instead of a cyclic prefix to provide a guard interval [29]. Therefore, reduced-CP and ZP-OTFS can reduce the overhead associated with full-CP transmission, but they use different guard structures and lead to different interference characteristics. In all cases, if the channel delay exceeds the available guard interval, interference may occur. A quantitative comparison of these schemes in the guard-violating regime is beyond the scope of this work and is left for future research.

8. Conclusions

This paper presents an analytical evaluation of CP-OTFS ISAC under high-Doppler and large-delay conditions, with explicit consideration of cyclic-prefix violation. Closed-form expressions are derived for the DD-domain matched-filter statistics, main-lobe energy, sidelobe floor, PSLR, ISLR, and EVM. The results show that when the target delay exceeds the cyclic prefix, additional interference increases the sidelobe floor. Consequently, the radar PSLR degrades, and this degradation cannot be fully compensated by increasing the SNR. The close agreement between theory and simulations validates the proposed analytical framework. These expressions provide useful tools for understanding and designing CP-OTFS ISAC systems, especially when the expected target delay may exceed the cyclic-prefix duration. From a practical design perspective, the proposed expressions can be used to predict the radar PSLR and communication EVM for given delay, Doppler, SNR, and CP parameters. They can therefore assist in selecting the CP duration according to the expected maximum delay, while accounting for the trade-off between CP protection and spectral efficiency. Future work will address multi-target and multipath scenarios, alternative pulse-shaping/windowing functions, CP-violation interference cancellation, and joint radar-communication optimization.

Author Contributions: Writing—original draft, S.H.; Writing—review and editing, J.-Y.B., S.M. and A.C.; Supervision, J.-Y.B., S.M. and A.C. All authors have read and agreed to the published version of the manuscript.

Funding: This research received no external funding.

Data Availability Statement: The original contributions presented in this study are included in the article. Further inquiries can be directed to the corresponding author.

Acknowledgments: ChatGPT 5 (OpenAI) was used only for minor English corrections. It was not used to generate scientific content or results.

Conflicts of Interest: The authors declare no conflicts of interest.

Appendix A. Derivation of the Average DD-Map Energy

This appendix provides the derivation of the average delay-Doppler (DD) map energy used in Section 3. The objective is to derive a closed-form expression for $\mathbb{E}\left[|Z_{\mathrm{DD}}[l'',k'']|^2\right]$, which serves as the analytical basis for the main-lobe energy, the sidelobe floor, the PSLR, and the ISLR.

The DD-domain matched-filter output is decomposed into a signal contribution and a noise contribution as

$$Z_{\mathrm{DD}}[l'',k''] = Z_{\mathrm{DD}}^{(s)}[l'',k''] + Z_{\mathrm{DD}}^{(b)}[l'',k''], \tag{A1}$$

where $Z_{\mathrm{DD}}^{(s)}[l'',k'']$ denotes the target echo contribution, and $Z_{\mathrm{DD}}^{(b)}[l'',k'']$ denotes the additive-noise contribution. By combining (2), (4), (6) and (7), the received TF-domain signal is obtained as the sum of two integrals: the first corresponds to the contribution of the current CP-OTFS sub-symbol, while the second accounts for the contribution of the previous sub-symbol. Substituting this result into the matched-filter expression (12) and then applying the SFFT in (13) gives the signal contribution as

$$\begin{aligned} Z_{\mathrm{DD}}^{(s)}[l'',k''] = \frac{h\,e^{-j2\pi\nu\tau}}{(MN)^{3/2}} \sum_{k=0}^{N-1}\sum_{l=0}^{M-1}\sum_{k'=0}^{N-1}\sum_{l'=0}^{M-1} X_{\mathrm{DD}}[l,k]X_{\mathrm{DD}}^{*}[l',k'] \sum_{n=0}^{N-1}\sum_{m=0}^{M-1} e^{j2\pi\frac{n(k-k'-k'')}{N}} e^{j2\pi\frac{m(l'+l'')}{M}} \\ \times \left[\frac{1}{T}\int_{nT_s+\tau_{\mathrm{CP}}}^{(n+1)T_s} e^{j2\pi\nu t} e^{-j2\pi\frac{m}{T}(t-nT_s)} \left(\sum_{m'=0}^{M-1} e^{j2\pi m'\left(\frac{t-nT_s-\tau}{T}-\frac{l}{M}\right)}\right) dt \right. \\ \left. + e^{-j2\pi\frac{k}{N}}\frac{1}{T}\int_{nT_s+T_{\mathrm{CP}}}^{nT_s+\tau_{\mathrm{CP}}} e^{j2\pi\nu t} e^{-j2\pi\frac{m}{T}(t-nT_s)} \left(\sum_{m'=0}^{M-1} e^{j2\pi m'\left(\frac{t-(n-1)T_s-\tau}{T}-\frac{l}{M}\right)}\right) dt\right] \end{aligned} \tag{A2}$$

and

$$Z_{\mathrm{DD}}^{(b)}[l'',k''] = \frac{1}{NM}\sum_{n=0}^{N-1}\sum_{m=0}^{M-1}\sum_{k'=0}^{N-1}\sum_{l'=0}^{M-1} X_{\mathrm{DD}}^{*}[l',k'] e^{-j2\pi\left(\frac{nk'}{N}-\frac{ml'}{M}\right)} \frac{1}{T}\int_{nT_s+T_{\mathrm{CP}}}^{(n+1)T_s} b(t) e^{-j2\pi m\frac{t-nT_s}{T}} dt e^{-j2\pi\left(\frac{nk''}{N}-\frac{ml''}{M}\right)}. \tag{A3}$$

Since $b(t)$ is zero mean and statistically independent of the transmitted data symbols, the cross-term between the signal and noise contributions vanishes. Hence,

$$\mathbb{E}\left[\left|Z_{\mathrm{DD}}[l'',k'']\right|^2\right] = \mathbb{E}\left[\left|Z_{\mathrm{DD}}^{(s)}[l'',k'']\right|^2\right] + \mathbb{E}\left[\left|Z_{\mathrm{DD}}^{(b)}[l'',k'']\right|^2\right]. \tag{A4}$$

Using the noise statistics, the noise contribution is obtained as

$$\mathbb{E}\left[\left|Z_{\mathrm{DD}}^{(b)}[l'',k'']\right|^2\right] = \sigma_{\mathrm{X}}^2\sigma_b^2. \tag{A5}$$

The signal contribution (A2) is rewritten as

$$Z_{\mathrm{DD}}^{(s)}[l'',k''] = \sum_{l,k}\sum_{l',k'} X_{\mathrm{DD}}[l,k]X_{\mathrm{DD}}^{*}[l',k']C_{(l,k),(l',k')}(l'',k''), \tag{A6}$$

where $C_{(l,k),(l',k')}(l'',k'')$ denotes the deterministic coefficient multiplying $X_{\mathrm{DD}}[l,k]X_{\mathrm{DD}}^{*}[l',k']$ in (A2). It therefore collects the channel coefficient, the delay- and Doppler-dependent phase terms, the finite sums, and the two time-domain integrals appearing in (A2).

Taking the squared magnitude and averaging gives

$$\begin{aligned} \mathbb{E}\left[\left|Z_{\mathrm{DD}}^{(s)}[l'',k'']\right|^2\right] = \sum_{l,k}\sum_{l',k'}\sum_{p,q}\sum_{p',q'} \mathbb{E}\left[X_{\mathrm{DD}}[l,k]X_{\mathrm{DD}}^{*}[l',k']X_{\mathrm{DD}}^{*}[p,q]X_{\mathrm{DD}}[p',q']\right] \\ \times C_{(l,k),(l',k')}(l'',k'')C_{(p,q),(p',q')}^{*}(l'',k''). \end{aligned} \tag{A7}$$

Using the fourth-order moment–cumulant relation for i.i.d. zero-mean proper complex symbols, only the admissible index pairings remain due to statistical independence. The resulting fourth-order moment is therefore

$$\begin{aligned} \mathbb{E}\left[X_{\mathrm{DD}}[l,k]X_{\mathrm{DD}}^{*}[l',k']X_{\mathrm{DD}}^{*}[p,q]X_{\mathrm{DD}}[p',q']\right] = \sigma_a^4\delta_{l,l'}\delta_{k,k'}\delta_{p,p'}\delta_{q,q'} + \sigma_a^4\delta_{l,p}\delta_{k,q}\delta_{l',p'}\delta_{k',q'} \\ + \left(\mu_a^4 - 2\sigma_a^4\right)\delta_{l,l'}\delta_{k,k'}\delta_{l,p}\delta_{k,q}\delta_{l,p'}\delta_{k,q'}. \end{aligned} \tag{A8}$$

Substituting (A8) into (A7), the average signal energy is decomposed into three terms:

$$\mathbb{E}\left[\left|Z_{\mathrm{DD}}^{(s)}[l'',k'']\right|^2\right] = S_1 + S_2 + S_3. \tag{A9}$$

The first term is

$$S_1 = \sigma_a^4 \sum_{l,k} \sum_{l',k'} \left|C_{(l,k),(l',k')}(l'',k'')\right|^2. \tag{A10}$$

After evaluating the sums over the Doppler indices and the time-domain integrals, this term becomes, using (21) and (22),

$$S_1 = \frac{\sigma_a^4 |h|^2}{M^2} \sum_{l=0}^{M-1} \sum_{m=0}^{M-1} \left(|\Phi_A(l,m)|^2 + |\Phi_B(l,m)|^2\right). \tag{A11}$$

The second term is the coherent contribution:

$$S_2 = \sigma_a^4 \left|\sum_{l,k} C_{(l,k),(l,k)}(l'',k'')\right|^2. \tag{A12}$$

By using the finite-sum identities in the Doppler and delay dimensions, this term is obtained as

$$S_2 = \frac{\sigma_a^4 |h|^2}{MN} \mathcal{G}(\nu, \tau_{\mathrm{CP}}) \left|\mathcal{D}_N\left(\nu T_s - \frac{k''}{N}\right)\right|^2 \left|\mathcal{D}_M\left(\frac{l''}{M} - \frac{\tau}{T}\right)\right|^2. \tag{A13}$$

The third term is associated with the fourth-order moment correction:

$$S_3 = \left(\mu_a^4 - 2\sigma_a^4\right) \sum_{l,k} \left|C_{(l,k),(l,k)}(l'',k'')\right|^2. \tag{A14}$$

It is given by

$$S_3 = \frac{\mu_a^4 - 2\sigma_a^4}{M^3 N^2} |h|^2 \left|\mathcal{D}_N\left(\nu T_s - \frac{k''}{N}\right)\right|^2 \sum_{l=0}^{M-1} \left(|\Psi_A(l,m)|^2 + |\Psi_B(l,m)|^2\right). \tag{A15}$$

Combining (A9), (A11), (A13) and (A15), the average signal energy is

$$\begin{aligned} \mathbb{E}\left[\left|Z_{\mathrm{DD}}^{(s)}[l'',k'']\right|^2\right] = {} & \frac{\sigma_a^4 |h|^2}{M^2} \sum_{l=0}^{M-1} \sum_{m=0}^{M-1} \left(|\Phi_A(l,m)|^2 + |\Phi_B(l,m)|^2\right) + \frac{\sigma_a^4 |h|^2}{MN} \mathcal{G}(\nu, \tau_{\mathrm{CP}}) \left|\mathcal{D}_N\left(\nu T_s - \frac{k''}{N}\right)\right|^2 \left|\mathcal{D}_M\left(\frac{l''}{M} - \frac{\tau}{T}\right)\right|^2 \\ & + \frac{\mu_a^4 - 2\sigma_a^4}{M^3 N^2} |h|^2 \left|\mathcal{D}_N\left(\nu T_s - \frac{k''}{N}\right)\right|^2 \sum_{l=0}^{M-1} \left(|\Psi_A(l,m)|^2 + |\Psi_B(l,m)|^2\right). \end{aligned} \tag{A16}$$

It remains to add the noise contribution (A5) into (A16) to obtain the total average DD-map energy.

Appendix B. Derivation of the EVM Expression

The average squared EVM is written as

$$\begin{aligned} \gamma_{\mathrm{EVM}}^2 &= \frac{1}{MN\sigma_X^2} \sum_{k'=0}^{N-1} \sum_{l'=0}^{M-1} \mathbb{E}\left[\left|\widehat{X}_{\mathrm{DD}}[k',l'] - X_{\mathrm{DD}}[k',l']\right|^2\right] \\ &= \frac{1}{MN\sigma_X^2} \sum_{k'=0}^{N-1} \sum_{l'=0}^{M-1} \left(\mathbb{E}\left[\left|\widehat{X}_{\mathrm{DD}}[k',l']\right|^2\right] + \mathbb{E}\left[\left|X_{\mathrm{DD}}[k',l']\right|^2\right] - 2\Re\left\{\mathbb{E}\left[\widehat{X}_{\mathrm{DD}}[k',l']\overline{X}_{\mathrm{DD}}[k',l']\right]\right\}\right). \end{aligned} \tag{A17}$$

Substituting the received TF-domain signal into (A17) gives

$$\widehat{X}_{\mathrm{DD}}[k',l'] = b[k',l'] + \frac{1}{NM}\sum_{m=0}^{M-1}\sum_{n'=0}^{N-1}\sum_{m'=0}^{M-1}\sum_{k=0}^{N-1}\sum_{l=0}^{M-1} X_{\mathrm{DD}}[k,l]e^{j2\pi\left(\frac{ml'}{M}-\frac{m'l}{M}\right)}e^{j2\pi\frac{n'(k-k')}{N}}e^{-j2\pi m'\frac{\tau}{T}}e^{j2\pi m\frac{\tau}{T}}e^{j2\pi\nu n'T_s} \times\left[K(\pi(m'-m+\nu T))+\left(e^{-j2\pi\frac{k'}{N}}e^{j2\pi m'\frac{T_s}{T}}e^{j2\pi\nu T_s}-1\right)\frac{\tau_{\mathrm{CP}}-T_{\mathrm{CP}}}{T}K\left(\pi(m'-m+\nu T)\frac{\tau_{\mathrm{CP}}-T_{\mathrm{CP}}}{T}\right)\right], \tag{A18}$$

where $K(u) = e^{ju}\,\mathrm{sinc}(u)$.

The three terms in (A17) are evaluated separately. The first term, the average received-symbol, energy is

$$\frac{1}{MN}\sum_{k'=0}^{N-1}\sum_{l'=0}^{M-1}\mathbb{E}\left[\left|\widehat{X}_{\mathrm{DD}}[k',l']\right|^2\right] = \sigma_b^2+\sigma_X^2\mathcal{A}_M, \tag{A19}$$

where

$$\mathcal{A}_M = \sum_{m=-M+1}^{M-1}\left(1-\frac{|m|}{M}\right)\left[\left|K(\pi(m+\nu T))-\frac{\tau_{\mathrm{CP}}-T_{\mathrm{CP}}}{T}K\left(\pi(m+\nu T)\frac{\tau_{\mathrm{CP}}-T_{\mathrm{CP}}}{T}\right)\right|^2 + \left|\frac{\tau_{\mathrm{CP}}-T_{\mathrm{CP}}}{T}K\left(\pi(m+\nu T)\frac{\tau_{\mathrm{CP}}-T_{\mathrm{CP}}}{T}\right)\right|^2\right]. \tag{A20}$$

The second term is simply the mean transmitted-symbol energy, which is equal to 1 by definition. The third term, the transmitted–received cross-correlation term, is

$$\Re\left\{\sum_{k'=0}^{N-1}\sum_{l'=0}^{M-1}\mathbb{E}\left[\widehat{X}_{\mathrm{DD}}[k',l']\overline{X}_{\mathrm{DD}}[k',l']\right]\right\} = \sigma_X^2\mathcal{D}_M\left(\frac{\tau}{T}\right)\mathcal{D}_N(\nu T_s)\sqrt{\mathcal{G}(\nu,\tau_{\mathrm{CP}})} \times\cos\left[\pi\left((N-1)\nu T_s-(M-1)\frac{\tau}{T}+\nu T\left(1+\frac{\tau_{\mathrm{CP}}-T_{\mathrm{CP}}}{T}\right)\right)\right]. \tag{A21}$$

Combining the three terms into (A17) gives the exact finite-M EVM:

$$\gamma_{\mathrm{EVM}}^2 = \frac{\sigma_b^2}{\sigma_X^2}+1+\sum_{m=-M+1}^{M-1}\left(1-\frac{|m|}{M}\right)\left[\left|K(\pi(m+\nu T))-\frac{\tau_{\mathrm{CP}}-T_{\mathrm{CP}}}{T}K\left(\pi(m+\nu T)\frac{\tau_{\mathrm{CP}}-T_{\mathrm{CP}}}{T}\right)\right|^2 + \left|\frac{\tau_{\mathrm{CP}}-T_{\mathrm{CP}}}{T}K\left(\pi(m+\nu T)\frac{\tau_{\mathrm{CP}}-T_{\mathrm{CP}}}{T}\right)\right|^2\right] - 2\frac{1}{M}\mathcal{D}_M\left(\frac{\tau}{T}\right)\frac{1}{N}\mathcal{D}_N(\nu T_s) \times\sqrt{\mathcal{G}(\nu,\tau_{\mathrm{CP}})}\cos\left[\pi\left((N-1)\nu T_s-(M-1)\frac{\tau}{T}+\nu T\left(1+\frac{\tau_{\mathrm{CP}}-T_{\mathrm{CP}}}{T}\right)\right)\right]. \tag{A22}$$

We observe that

$$\lim_{M\to\infty}\mathcal{A}_M = 1. \tag{A23}$$

Then, in practice and for finite M, the approximation is used.

References

1. Liu, F.; Masouros, C.; Petropulu, A.P.; Griffiths, H.; Hanzo, L. Joint radar and communication design: Applications, state-of-the-art, and the road ahead. *IEEE Trans. Commun.* **2020**, *68*, 3834–3862. [CrossRef]
2. Zhang, J.A.; Rahman, M.L.; Wu, K.; Huang, X.; Guo, Y.J.; Chen, S.; Yuan, J. Enabling joint communication and radar sensing in mobile networks—A survey. *IEEE Commun. Surv. Tutor.* **2022**, *24*, 306–345. [CrossRef]

3. Hadani, R.; Rakib, S.; Tsatsanis, M.; Monk, A.; Goldsmith, A.J.; Molisch, A.F.; Calderbank, R. Orthogonal time frequency space modulation. In *Proceedings of the IEEE Wireless Communications and Networking Conference (WCNC), San Francisco, CA, USA*; IEEE: Piscataway, NJ, USA , 2017; pp. 1–6.
4. Wei, Z.; Yuan, W.; Li, S.; Yuan, J.; Bharatula, G.; Hadani, R.; Hanzo, L. Orthogonal time-frequency space modulation: A promising next-generation waveform. *IEEE Wirel. Commun.* **2021**, *28*, 136–144. [CrossRef]
5. Yuan, W.; Wei, Z.; Li, S.; Schober, R.; Caire, G. Orthogonal time frequency space modulation—Part III: ISAC and potential applications. *IEEE Commun. Lett.* **2023**, *27*, 14–18. [CrossRef]
6. Yuan, W.; Wei, Z.; Li, S.; Yuan, J.; Ng, D.W.K. Integrated sensing and communication-assisted orthogonal time frequency space transmission for vehicular networks. *IEEE J. Sel. Top. Signal Process.* **2021**, *15*, 1515–1528. [CrossRef]
7. Yuan, W.; Zhou, L.; Dehkordi, S.K.; Li, S.; Fan, P.; Caire, G.; Poor, H.V. From OTFS to DD-ISAC: Integrating sensing and communications in the delay-Doppler domain. *IEEE Wirel. Commun.* **2024**, *31*, 152–160. [CrossRef]
8. Marchese, M.; Wymeersch, H.; Spallaccini, P.; Savazzi, P. Progressive Inter-Path Interference Cancellation Algorithm for Channel Estimation Using Orthogonal Time–Frequency Space. *Sensors* **2024**, *24*, 4414. [CrossRef]
9. Karpovich, P.; Zielinski, T.P. Integrated Sensing and Communication Using Random Padded OTFS with Reduced Interferences. *Sensors* **2025**, *25*, 4816. [CrossRef]
10. Nie, M.; Chong, R.; Li, S.; Farhang, A.; Göttsch, F.; Ng, D.W.K.; Matthaiou, M.; Li, Y. Toward Standardizing OTFS: A Candidate Waveform for Next-Generation Wireless Networks. *IEEE Commun. Stand. Mag.* **2026**, *10*, 107–118. [CrossRef]
11. Li, S.; Lu, G.; Zhen, L.; Feng, D.; Yu, K.; Ng, D.W.K. Block-Cyclic Zadoff–Chu Sequences-Based Preamble Design and Detection for OTFS-Enabled LEO Satellite Random Access Systems. *IEEE Trans. Veh. Technol.* **2026**, *75*, 5179–5184. [CrossRef]
12. Gaudio, L.; Kobayashi, M.; Caire, G.; Colavolpe, G. On the effectiveness of OTFS for joint radar parameter estimation and communication. *IEEE Trans. Wirel. Commun.* **2020**, *19*, 5951–5965. [CrossRef]
13. Raviteja, P.; Phan, K.T.; Hong, Y.; Viterbo, E. Orthogonal time frequency space (OTFS) modulation based radar system. In *Proceedings of the IEEE Radar Conference, Boston, MA, USA*; IEEE: Piscataway, NJ, USA, 2019; pp. 1–6.
14. Dayarathna, S.; Smith, P.J.; Senanayake, R.; Evans, J. OTFS based joint radar and communication: Signal analysis using the ambiguity function. *IEEE Signal Process. Lett.* **2024**, *31*, 919–923. [CrossRef]
15. Berger, C.R.; Demissie, B.; Heckenbach, J.; Willet, P.; Zhou, S. Signal processing for passive radar using OFDM waveforms. *IEEE J. Sel. Top. Signal Process.* **2010**, *4*, 226–238. [CrossRef]
16. Teng, Z.; An, J.; Gan, L.; Al-Dhahir, N.; Han, Z. Flexible intelligent metasurface for enhancing multi-target wireless sensing. *IEEE Trans. Veh. Technol.* **2025**, *74*, 19825–19830. [CrossRef]
17. Hamrouni, S.; Baudais, J.-Y.; Méric, S.; Cherif, A. Analytical PSLR and ISLR expressions for OTFS radar performance evaluation. In *Proceedings of the European Radar Conference, London, UK*; IEEE: Piscataway, NJ, USA, 2026 .
18. Raviteja, P.; Phan, K.T.; Hong, Y.; Viterbo, E. Interference cancellation and iterative detection for orthogonal time frequency space modulation. *IEEE Trans. Wirel. Commun.* **2018**, *17*, 6501–6515. [CrossRef]
19. Keskin, M.F.; Wymeersch, H.; Alvarado, A. Radar sensing with OTFS: Embracing ISI and ICI to surpass the ambiguity barrier. In *Proceedings of the IEEE International Conference on Communications Workshops (ICC Workshops), Virtual Conference*; IEEE: Piscataway, NJ, USA, 2021; pp. 1–6.
20. Keskin, M.F.; Marcus, C.; Eriksson, O.; Alvarado, A.; Widmer, J.; Wymeersch, H. Integrated sensing and communications with MIMO-OTFS: ISI/ICI exploitation and delay-Doppler multiplexing. *IEEE Trans. Wirel. Commun.* **2024**, *23*, 10229–10246. [CrossRef]
21. Tang, Z.; Yu, L. A method of interference suppression in integrated OTFS communication and sensing systems. *IEEE Access* **2024**, *12*, 144044–144054. [CrossRef]
22. Farhang, A.; RezazadehReyhani, A.; Doyle, L.E.; Farhang-Boroujeny, B. Low complexity modem structure for OFDM-based orthogonal time frequency space modulation. *IEEE Wirel. Commun. Lett.* **2018**, *7*, 344–347. [CrossRef]
23. Baudais, J.-Y.; Méric, S.; Benmeziane, B.; Cinglant, K. Doppler robustness of joint communication and radar systems using the Wiener filter. *IEEE Trans. Commun.* **2023**, *71*, 4807–4818. [CrossRef]
24. Raviteja, P.; Hong, Y.; Viterbo, E.; Biglieri, E. Practical pulse-shaping waveforms for reduced-cyclic-prefix OTFS. *IEEE Trans. Veh. Technol.* **2019**, *68*, 957–961. [CrossRef]
25. Tiwari, S.; Das, S.S. Circularly pulse-shaped orthogonal time frequency space modulation. *Electron. Lett.* **2020**, *56*, 157–160. [CrossRef]
26. Mei, C.; Zhang, W. Optimal design of OTFS systems for fractional inter-Doppler interference suppression. *IEICE Trans. Commun.* **2025**, *E108-B*, 431–439. [CrossRef]
27. Tusha, A.; Arslan, H. Low complex inter-Doppler interference mitigation for OTFS systems via global receiver windowing. *IEEE Trans. Veh. Technol.* **2023**, *72*, 7685–7698. [CrossRef]

28. Huang, Y.; Rao, B.D. Awareness of channel statistics for slow cyclic prefix adaptation in an OFDMA system. *IEEE Wirel. Commun. Lett.* **2012**, *1*, 332–335. [CrossRef]
29. Thaj, T.; Viterbo, E. Low complexity iterative rake decision feedback equalizer for zero-padded OTFS systems. *IEEE Trans. Veh. Technol.* **2020**, *69*, 15606–15622. [CrossRef]

Disclaimer/Publisher's Note: The statements, opinions and data contained in all publications are solely those of the individual author(s) and contributor(s) and not of MDPI and/or the editor(s). MDPI and/or the editor(s) disclaim responsibility for any injury to people or property resulting from any ideas, methods, instructions or products referred to in the content.